Hydrodynamic performance of a rim-driven thruster improved with gap geometry adjustment

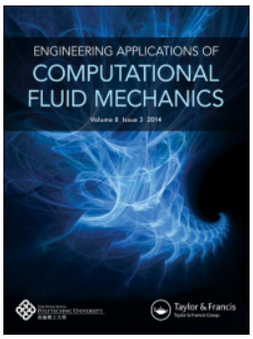

Taylor & Francis
Taylor & Francis Group

Engineering Applications of Computational Fluid Mechanics

ISSN: (Print) (Online) Journal homepage: https://www.tandfonline.com/loi/tcfm20

Hydrodynamic performance of a rim-driven thruster improved with gap geometry adjustment

Jianfeng Lin, Hua-Dong Yao, Chao Wang, Yumin Su & Chun Yang

To cite this article: Jianfeng Lin, Hua-Dong Yao, Chao Wang, Yumin Su & Chun Yang (2023) Hydrodynamic performance of a rim-driven thruster improved with gap geometry adjustment, Engineering Applications of Computational Fluid Mechanics, 17:1, 2183902, DOI: 10.1080/19942060.2023.2183902

To link to this article: https://doi.org/10.1080/19942060.2023.2183902

Published online: 13 Mar 2023.

ENGINEERING APPLICATIONS OF COMPUTATIONAL FLUID MECHANICS
2023, VOL. 17, NO. 1, 2183902
https://doi.org/10.1080/19942060.2023.2183902

Taylor & Francis
Taylor & Francis Group

Hydrodynamic performance of a rim-driven thruster improved with gap geometry adjustment

Jianfeng Lin [a,b], Hua-Dong Yao [b], Chao Wang [a], Yumin Su[a] and Chun Yang[a]

[a]College of Shipbuilding Engineering, Harbin Engineering University, Harbin, People's Republic of China; [b]Department of Mechanics and Maritime Sciences, Chalmers University of Technology, Gothenburg, Sweden

ABSTRACT

The hubless rim-driven thruster (RDT) has become increasingly interesting for ship propulsion. Gap flow has been proven as the main feature of RDT that cannot be simply neglected. In this study, based on a classical hubless RDT, the effects of the gap geometry are studied by adjusting its axial passage length, and inlet and outlet oblique angles. The hydrodynamic characteristics of the RDT were simulated with OpenFOAM based on the $k-\omega$ shear stress transport turbulence model. Due to the pressure increase after the main flow passes through the rotating blades, the flow inside gap is driven upstream, which is opposite to the main flow direction. It is found that the hydrodynamic efficiency is increased as the gap axial passage length is shortened, which is realized by increasing the oblique angle with the fixed inlet and outlet positions. Moving the inlet and outlet to further downstream and upstream positions has negligible effects on the hydrodynamic efficiency and leads to recirculating flow within the gap near its inlet. These findings shed light on the design of the gap geometry to improve the RDT hydrodynamic performance.

ARTICLE HISTORY
Received 18 November 2022
Accepted 19 February 2023

KEYWORDS
Hubless rim-driven thruster; gap flow; hydrodynamic performance; numerical simulation

1. Introduction

As international maritime transactions have increased, there has been a daily increase in the demand for ship capacity and propulsion power (Lin et al., 2022b). The drawbacks of traditional ship propulsion systems have gradually become apparent. The main engine's size and power increase in tandem with the demand for propulsion power. The structural design of the propulsion shaft system is also more complex, increasing ship design difficulty and construction costs, reducing ship space utilization and worsening propulsion efficiency (Su et al., 2020). In this situation, the concept of a rim-driven thruster (RDT) arose.

The RDT is a novel type of integrated motor thruster, commonly known as a shaftless propeller. The torque driving the propeller blades of the RDT is provided by a circular rim that is structurally attached to the blade tips, as opposed to a traditional propeller, which is powered via its shaft (Grűmmer, 2016). The permanent magnet rotor is embedded in the rim at the top of the blade, and the motor stator is positioned in the duct or nozzle. The stator and rotor of the motor are assembled independently so that they are totally surrounded by seawater, which cools them in the gap. Furthermore, the RDT does not need water-tight treatment for rotational movements.

Using the rim to drive the propeller brings about benefits in several aspects. By incorporating an electric motor into the rim, a compact design with decreased weight and space occupation is accomplished. The transmission loss associated with the hub and the corresponding accessories (seals, bearings, and gearboxes) is eliminated, increasing mechanical efficiency. Furthermore, the system's maintenance is simplified. The hydrodynamic efficiency is improved. RDT, as investigated by Lea et al. (2003), is more economical than traditional propellers. The efficiency varies little depending on the operation circumstances. Because the water travelling through the rim efficiently transfers heat, no special cooling mechanisms are required. This results in minimal power usage. The environmental impact of noise has considerably decreased. The simple electric method generates far less noise and vibration than the traditional mechanical system with the hub and gearbox. Furthermore, because the blade tips are positioned on the rim, the hydrodynamic noise created by propeller tip vortices is avoided. Long fibres (e.g. floating fishing nets or ropes) jammed in the hub do little damage. As a result, the hubless type RDT may be used in challenging water environments.

Kort (1940) proposed the first RDT concept model in a patent. Additional RDT patents were established

CONTACT Chao Wang wangchao0104@hrbeu.edu.cn

following Kort's work, but all of them focused exclusively on the description of the broad concept of the device, without addressing the design of the machine itself or its performance (Yan et al., 2017). Although the concept of RDT has been presented for decades, it has only recently become a reality due to breakthroughs in materials, electric powertrains, and three-dimensional (3D) printing. In recent years, an increasing number of researches have been conducted to explore RDT technology, and some results have been applied to ship operations. Yakovlev et al. (2011) compared the open water characteristics of RDTs with and without hubs through model experiments. Cao et al. (2012) adopted the Reynolds Averaged Navier – Stokes (RANS) equations to analyze the case of four distinct propeller blades, and the numerical results revealed that the greatest radial circulation is observed at the blade tip. Song et al. (2015) examined four pairs of hub-type and hubless RDTs with varied hub diameters. The simulation findings demonstrated that hubless RDTs are more efficient than hub-type RDTs. The hubless RDTs provide more thrust and torque while having a lower thrust ratio (the ratio of the blades' thrust coefficient to the sum of the blades' and duct's thrust coefficients). Dubas et al. (2015) compared Re-Normalisation Group $k-\epsilon$ and $k-\omega$ Shear Stress Transport (SST) turbulence models and reported that the $k-\omega$ SST model is more robust in dealing with RDT-stator interactions at low advance ratios. Gaggero (2020) established a simulation-based design optimization method for changing the RDT blade shape to enhance propulsion performance and decrease cavitation. Song et al. (2020) used the computational fluid dynamics (CFD) approach to investigate each of the major influencing aspects of the RDT's hydrodynamic performance, including the aspect ratio of duct, diffusion ratio, contraction ratio of duct and tip diameter ratio of blade. Zhu and Liu (2022) investigated the RDT's external characteristics using experimental techniques and studied the inner flow characteristics using numerical simulation methods, revealing the flow loss mechanism. et al. (2022a; 2022b) simulated the effect of several transition turbulence models on the RDT's hydrodynamic performance prediction.

According to the above literature research, most previous studies have focused on optimizing the hydrodynamic characteristics of the propeller and duct profile of the RDT. However, the influence of the RDT's gap flow between the rotor and stator on its hydrodynamic performance cannot be ignored. Cao et al. (2014) investigated the effect of radial and axial gap sizes on flow variables by comparing gap flow fields with and without a propeller, as well as the effect on the hydrodynamic performance of RDT. The simulation results show that enlarging the gap width increases the frictional torque coefficient on the rim surface. Liu and Vanierschot (2021) employed a moving reference frame (MRF) technique to analyze the hydrodynamic performance of ducted propeller and RDT with gap flow. They found that the presence of the rim and induced gap flow have far more negative than positive influences on the RDT's hydrodynamic performance, leading to a significant reduction in efficiency when contrasted to the ducted propeller. Zhai et al. (2022) conducted an optimal design investigation of the duct for the RDT under the condition of considering the effect of the gap. The hydrodynamic characteristics of a counter-rotating RDT considering gap flow were investigated using the RANS method by Jiang et al. (2022). The torque computed with the inclusion of the gap friction deviates from the empirical formulae by more than 10%.

The current research for the gap flow of RDT is only focused on the gap width, and there is no improvement in the gap shape. Although empirical formulae can be used to modify the anticipated torque, the gap flow influence on the duct and propeller thrust is disregarded. In this study, a numerical investigation into the hydrodynamic performance of the RDT considering gap flow with various shapes is carried out using the RANS approach. This approach is generally cheaper than advanced CFD methods like large eddy simulation, as have been noticed based on canonical flow cases such as channel and turbulent boundary layer (Shao et al., 2022), rotating cylinders (Lin et al., 2022a), and RDT flow (Cao et al., 2012). The rest of this paper is structured as follows. Section 2 focuses on the governing equations, turbulence model, the RDT model with various shapes, boundary conditions, meshing, and verification of numerical methods used in this study. The results and discussion are reported in Section 3. And finally, Section 4 highlights the conclusions and offers recommendations for future investigations.

2. Methodology

2.1. Governing equations and turbulence model

The RANS equations for incompressible viscous flow are:

$$\frac{\partial U_i}{\partial x_i} = 0, \tag{1}$$

$$\frac{\partial U_i}{\partial t} + U_j \frac{\partial U_i}{\partial x_j} = -\frac{1}{\rho}\frac{\partial P}{\partial x_i} + \nu \frac{\partial^2 U_i}{\partial x_j \partial x_j} + S_j, \tag{2}$$

where U_i and U_j represent the mean velocity components ($i, j = 1, 2, 3$, standing for the component in the x, y, z direction), x_i and x_j represent the position vectors in tensor notation, ρ is the fluid density, t is the physical time,

P is the pressure, v is the kinematic viscosity coefficient, and S_j is the source term.

The computational domain is discretized using the finite volume method. The steady flow fields around the RDT are solved using the simpleFoam solvers in OpenFOAM. The governing equations are solved using the Gauss linear upwind convection schemes, the Gauss linear gradient schemes, the steady-state time discretization schemes, and the SIMPLE algorithm for pressure-velocity coupling. The MRF-based method implements the rotational motion of the rotor of the RDT. To accommodate non-orthogonal grids, numerical techniques for Laplacian and surface normal gradients are used. Relaxation factors are employed to control the solution's convergence. The convergence of the numerical simulation is guaranteed by controlling the iteration residuals to a standard of at least 10^{-7} for the continuity and momentum variables, indicating that the relative change of the magnitudes between iterations is less than this level. The k – ω SST model is utilized as a turbulence model to analyze the flow field with severe backpressure gradients while taking wall shear into consideration (Hu et al., 2022; Song et al., 2021; Yao & Davidson, 2019). The k – ω SST turbulence model has been proven by a number of experts to be a promising solution to the hydrodynamic problems of the RDT (Dubas et al., 2015; Gaggero, 2020; Song et al., 2015) and other rotating machinery (Ottersten et al., 2022a; 2022b). The transport equations for turbulent kinetic energy (k) and turbulence dissipation rate (ω) are described as (Lin et al., 2020; Menter et al., 2003):

$$\frac{\partial(\rho k)}{\partial t}+\frac{\partial(\rho U_i k)}{\partial x_i}=\widetilde{P}_k-\rho\beta^*\omega k+\frac{\partial}{\partial x_i}\left[(\mu+\sigma_k\mu_t)\frac{\partial k}{\partial x_i}\right], \quad (3)$$

$$\frac{\partial(\rho\omega)}{\partial t}+\frac{\partial(\rho U_i\omega)}{\partial x_i}=\alpha\rho S_r^2-\rho\beta\omega^2+\frac{\partial}{\partial x_i}\left[(\mu+\sigma_\omega\mu_t)\frac{\partial\omega}{\partial x_i}\right]+2(1-F_1)\rho\sigma_{\omega2}\frac{1}{\omega}\frac{\partial k}{\partial x_i}\frac{\partial\omega}{\partial x_i}, \quad (4)$$

where $\widetilde{P}_k$ is a production limiter used to keep turbulence from building up in stagnant areas, β^*, α, and β are constants for turbulence model, σ_k denotes the turbulent Prandtl numbers for k, μ_t denotes the turbulence viscosity, S_r denotes the invariant measure of the strain rate, σ_ω denotes the turbulent Prandtl numbers for ω, and F_1 denotes the blending function.

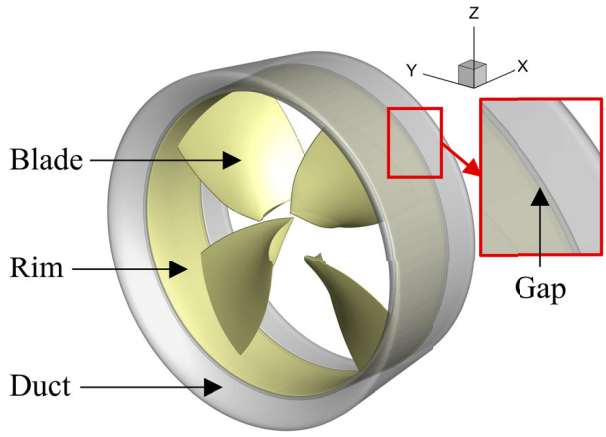

Figure 1. Geometry of the hubless RDT.

Table 1. Parameters of the RDT model.

Parameter	Unit	Value
Number of blades (Z)	–	4
Blade diameter (D_b)	m	0.25
Blade area ratio (λ_a)	–	0.7
Blade pitch ratio (λ_p)	–	1.0
Blade tip diameter (D_t)	m	0.05
Duct diameter (D_d)	m	0.3
Duct length (L_d)	m	0.125
Rim thickness (H)	m	0.006
Gap width (S)	m	0.0015

2.2. The RDT model with various shapes

The RDT model used in this study is based on the typical MARIN 19A duct and Ka 4–70 propeller. This combination is adopted by most RDT researches (Grűmmer, 2016; Jiang et al., 2022; Song et al., 2020). The rim gap is a common feature in RDT. While the gap dimensions are generally tiny, the gap impact on the thruster performance cannot be underestimated. The ratio of the initial gap form refers to the research of Liu and Vanierschot (2021). The main parameters and geometric structure of the RDT model used in this study are shown in Table 1 and Figure 1, respectively. In Table 1, the blade area ratio (λ_a) is defined as the ratio of the developed area of all blades to the disk area ($A_0=\pi D_b^2/4$), and the blade pitch ratio (λ_p) is defined as the ratio of the blade pitch to the blade diameter (D_b).

As shown in Figure 2, the variation parameters of the gap shape include the axial segment length of the gap (L_1) and the distance between the gap inlet and outlet (L_2). The gap width (S) is kept constant. Normally, the default value of oblique angle (θ) is equal to 90° so that the inlet and outlet are normal to the rotation axis. Initial values of rim length features L_1 and L_2 are equal to 0.066 m. In this work, θ is altered from 90° to 150° so as to investigate the effect of oblique gap shapes. Comparison studies are

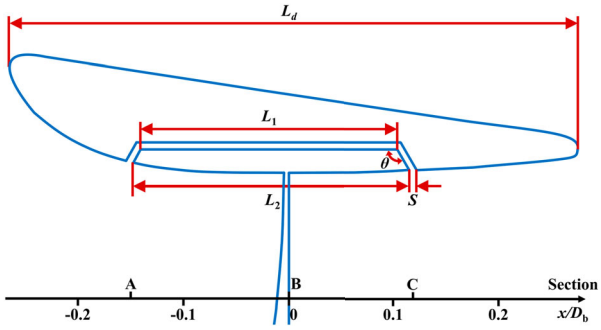

Figure 2. Geometric parameters of the gap.

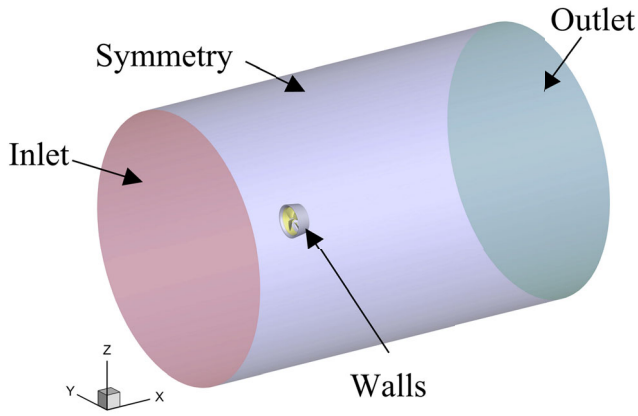

Figure 3. Computational domain and boundary conditions.

carried out by adjusting θ while keeping the variables L_1 or L_2 constant.

2.3. Boundary conditions and meshing

The computational domain of the RDT hydrodynamic simulation is a cylindrical shape with a diameter of 10 D_b and a length of 15 D_b, as shown in Figure 3. The size of the computational domain was verified to be sufficient by the previous work of Grümmer et al. (2017). The RDT model with no slip walls is arranged at the centre of the computational domain at 5 D_b from the velocity inlet and 10 D_b from the pressure outlet. The far field of the computational domain is specified as a symmetry surface. The rotational motion of the propeller is achieved by the MRF method, commonly used in RDT research (Dubas et al., 2015; Gaggero, 2020; Grűmmer, 2016; Song et al., 2015). The entire computational domain is calculated with the MRF method. It is worth noticing that the blades and the rim are the only two components that move with the rotating coordinate system, which is shown in yellow in Figure 2, and that the duct and far-field boundaries are stationary. The initial rotation coordinate system overlaps with the stationary coordinate system; the coordinate origin is at the geometric centre of the RDT; the coordinate axes' directions can be seen in Figure 3; and the rotation axis of the motion coordinate system is the x-axis.

The commercial software Pointwise was used to generate the unstructured mesh in the computational domain. Grid cell types include tetrahedrons, pyramids, and hexahedrons. Prism layers are generated near the RDT's walls, tetrahedrons in the flow field domain, and pyramids and hexahedrons for transitions at high skewness locations. It is critical to enhance calculation quality by refining certain regions of the computational domain. To be more specific, the mesh is gradually refined from the far field to the RDT walls, where the flow field is more disrupted, to provide a smooth transition between meshes of varying sizes and to suitably minimize the overall number of meshes. Furthermore, extra mesh refinement within the gap is necessary because the focus of this study is on the flow condition of the gap, as shown in Figure 4. The dimensionless wall distance Y+ value is kept approximately 1. The number of grid cell layers in the gap is 22 layers. The checkMesh command in OpenFOAM is used to evaluate the mesh quality, and no warnings and errors are found in the generated meshes. The maximum aspect ratio is 48.111, the maximum skewness is 2.566, and the cell growth ratio is 1.2.

2.4. Verification of numerical methods

This study employs the following hydrodynamic parameters, which are specified as follows:

$$J = V_a/(nD_b), \tag{5}$$

$$K_T = T/(\rho n^2 D_b^4), \tag{6}$$

$$K_Q = Q/(\rho n^2 D_b^5), \tag{7}$$

$$\eta = JK_T/(2\pi K_Q), \tag{8}$$

where J denotes the advance coefficient, V_a denotes the inflow velocity, n denotes the propeller rotation speed, K_T denotes the thrust coefficient, T denotes the thrust, K_Q denotes the torque coefficient, Q denotes the torque, and η denotes the efficiency of the RDT.

The results of the convergence analysis of the RDT meshes are listed in Table 2. The convergence analysis is performed at $J = 0.5$, $n = 7.5$ rps, and $\theta = 90°$. The accuracy of the simulations is evaluated by comparing the results of three meshes (approximately 8, 12, and 18 million cells) based on K_T and K_Q. The grid convergence index (GCI) method developed by Celik et al. (2008) is adopted to assess the discretization error of the RDT thrust and torque. The refinement ratio of the grid is

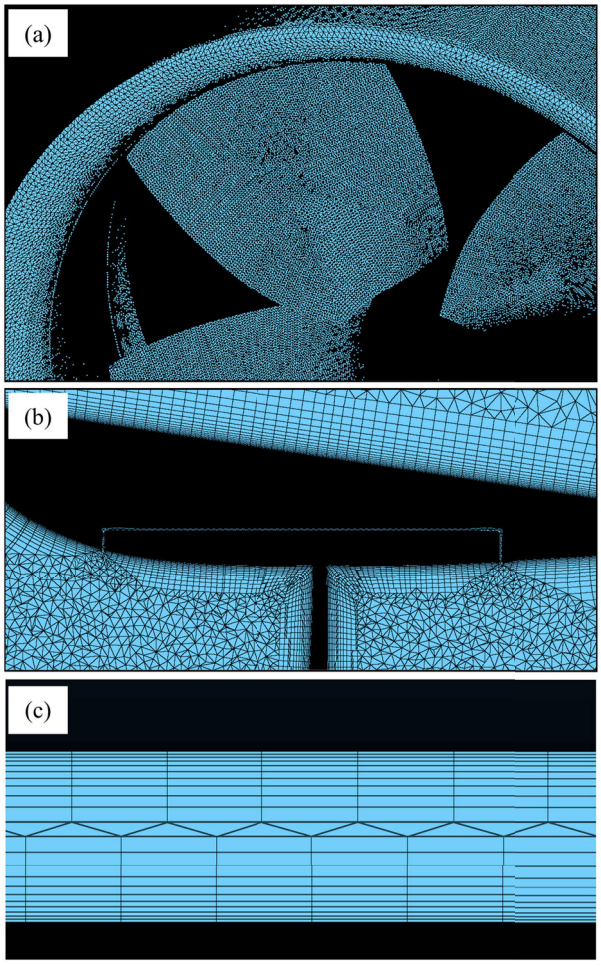

Figure 4. Mesh distribution: (a) surface mesh, (b) boundary layer, and (c) cells in the gap.

Table 2. Results of the grid convergence analysis.

	Total number of cells (millions)	K_T	GCI (%)	$10K_Q$	GCI (%)
Coarse	8	0.243	–	0.468	–
Medium	12	0.249	3.09	0.479	2.94
Fine	18	0.251	1.00	0.475	1.04

adopted as $\sqrt{2}$. The findings reveal that the GCI values of the fine grid are lower than those of the medium grid for both thrust and torque, demonstrating that the numerical uncertainty decreases as the grid is refined. The largest numerical uncertainty is claimed to be within 3.09% and 1.04% for the medium and fine grids, respectively. The fine grid is utilized as the final grid in this investigation based on the grid convergence analysis.

3. Results and discussion

Since there is a lack of systematic and comprehensive experimental results for the RDT used in this work, a similar result was used for comparison. CFD results for

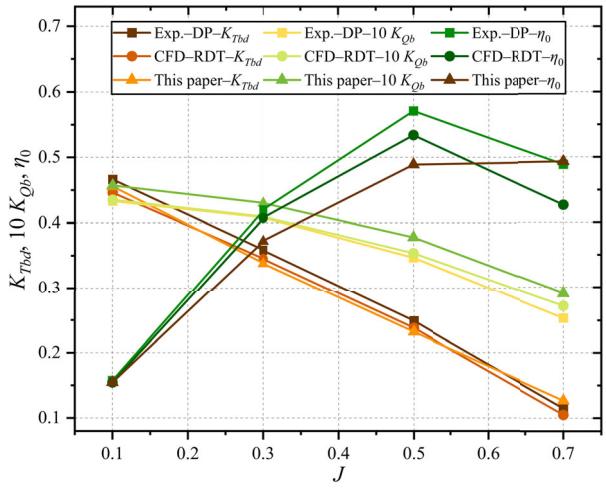

Figure 5. Comparison of open water characteristics between CFD and experimental results.

the same RDT but without considering the gap can be obtained from the literature (Song et al., 2020). Experimental results for a similar ducted propeller (DP) with the same MARIN 19A duct and Ka 4–70 propeller can be acquired from the publication (Baltazar et al., 2012). The experimental and numerical simulation results of the open water characteristics with and without considering a gap are compared as shown in Figure 5. The hydrodynamic coefficients for the comparison are the thrust coefficients of the blade and duct (K_{Tbd}), the torque coefficients of the blade (K_{Qb}), and the efficiency without considering the rim (η_0), respectively. When observing the thrust coefficient, a good consistency is noticed, which confirms the simulation code and the correct use of the blade and duct geometry selection. When comparing the torque coefficient results, a resembling trend can be noticed. The torque calculated by this study is overestimated over the whole range of advance coefficients. This bias is thought to be the result of comparative literatures not taking friction between the duct and the rim into account. In this situation, the overestimation of torque leads to low efficiency. The open water efficiency considering the gap is reduced by around 8% compared to the result without the gap. In addition, similar findings can be observed in the study of Liu and Vanierschot (2021). The efficiency of their numerical simulation of the RDT is about 15% lower than the experimental value of the DP at the high advance coefficient.

3.1. Fixed axial segment length of the gap – L_1

In this section, the gap oblique angles (θ) are selected at 15° intervals for numerical analysis to comprehensively investigate the effects of different positions of the

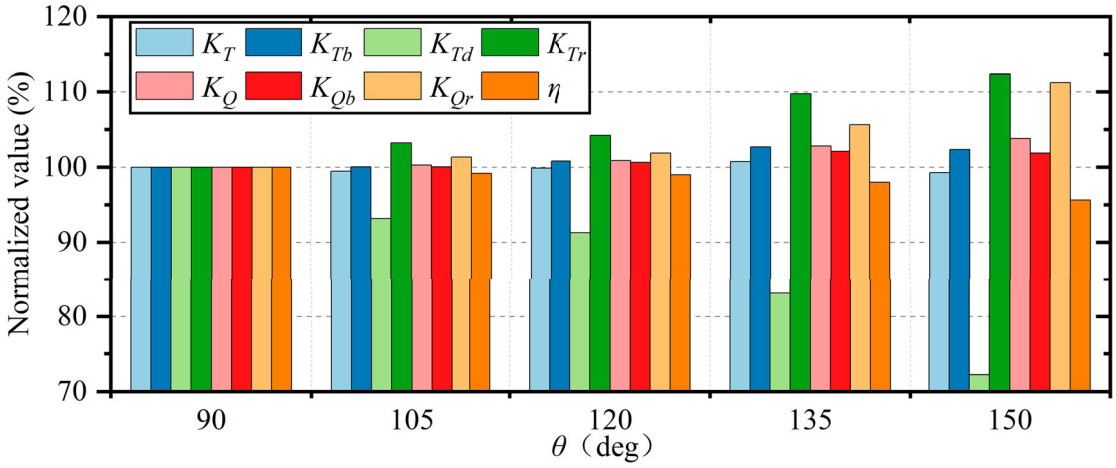

Figure 6. Hydrodynamic characteristics of the RDT at different oblique angles (θ) with a fixed axial segment length of the gap.

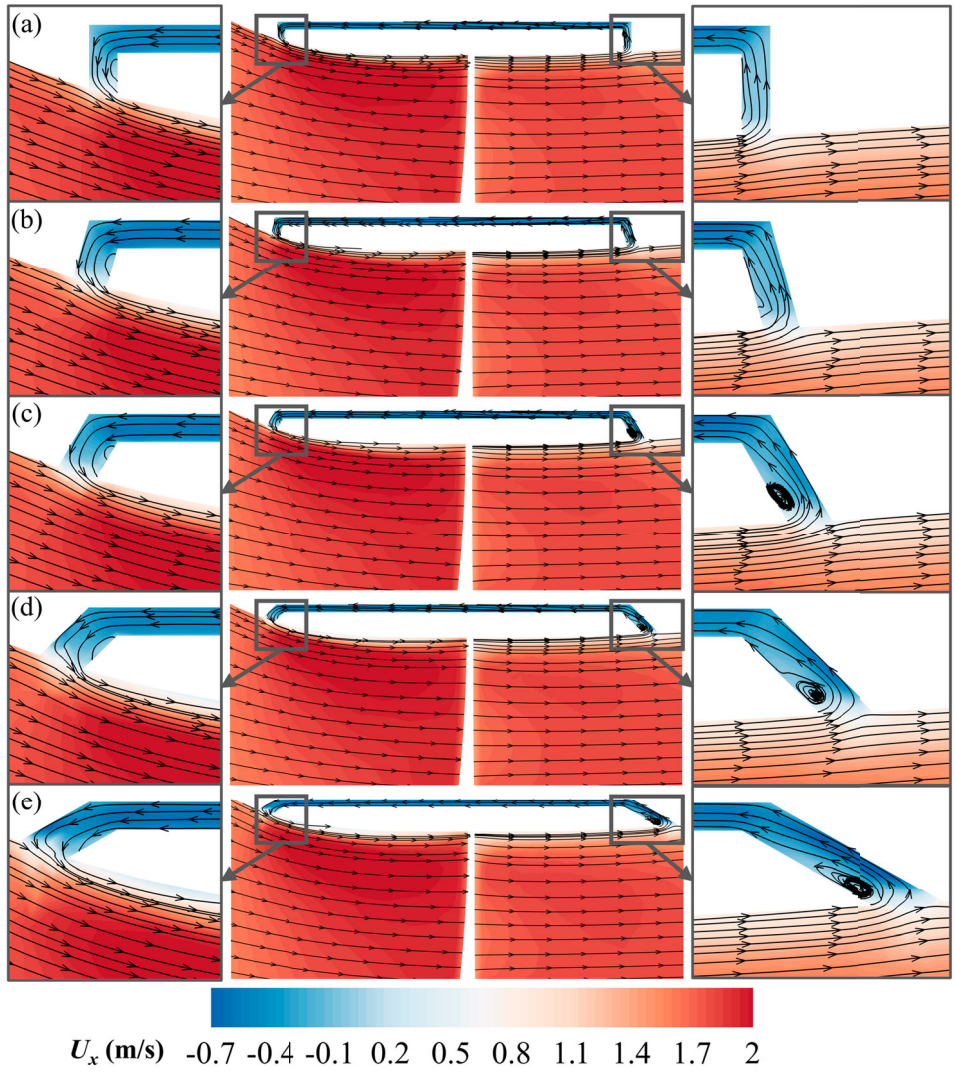

Figure 7. The axial velocity distribution of the flow field at different oblique angles (θ) with a fixed axial segment length of the gap: (a) $\theta = 90°$, (b) $\theta = 105°$, (c) $\theta = 120°$, (d) $\theta = 135°$, and (e) $\theta = 150°$.

inlet and outlet of the gap on the hydrodynamic performance of the RDT. The primary conditions of the numerical simulation are set: $J = 0.5$, $n = 7.5$ rps, and $L_1 = 0.066$ m. Figure 6 shows the hydrodynamic characteristics of the RDT at different θ with a fixed axial segment length of the gap. The individual hydrodynamic coefficients at different θ are normalized based on data at $\theta = 90°$. It is clear that the η reduces gradually as θ grows. The K_T of RDT increases at $\theta = 135°$, but the K_Q rises even more, which leads to a decrease in η instead. Through specifically examining the individual components of thrust and torque, it can be seen that as θ grows, all of the blade thrust coefficients (K_{Tb}), rim thrust coefficients (K_{Tr}), blade torque coefficients (K_{Qb}), and rim torque coefficients (K_{Qr}) increase while all of the duct thrust coefficients (K_{Td}) decrease. It is caused by the fact that as θ grows, the rim expands and the duct contracts.

Figure 7 illustrates the axial velocity (U_x) distribution of the flow field at different θ with a fixed axial segment length of the gap. It can be observed that the flow direction in the gap is the opposite to the incoming flow

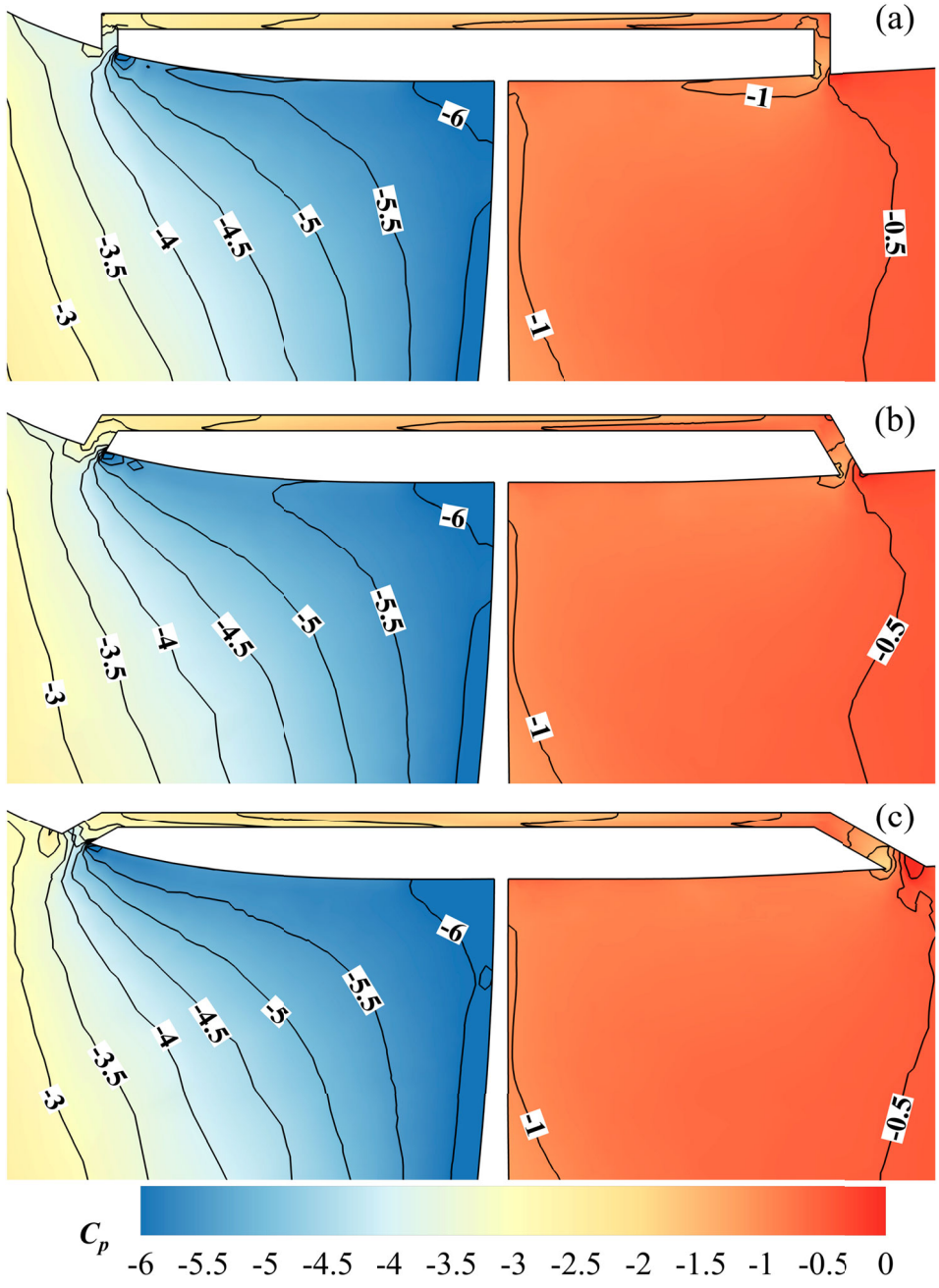

Figure 8. The pressure distribution of the flow field at different oblique angles (θ) with a fixed axial segment length of the gap: (a) $\theta = 90°$, (b) $\theta = 120°$, and (c) $\theta = 150°$.

direction. This can be expressed as a higher pressure at the downstream gap opening than at the upstream gap opening because the main flow is pressurized by the rotating blades, as shown in Figure 8. It is worth noting that the inlet of the gap flow is on the pressure side behind the blade and the outlet is on the suction side in front of the blade. It leads to a higher relative pressure at the inlet of the gap than at the outlet. The variation of θ changes not only the total length of the gap but also the inlet and outlet positions of the gap. As the inlet position of the gap moves toward the trailing edge of the duct, a small vortex gradually forms at the inlet of the gap. This could be one of the reasons for the reduced efficiency, which will be further analyzed in Section 3.2. At the outlet of the gap, the flow in the gap is carried by the incoming flow with higher velocity and merged to increase the stream velocity in front of the blade. As shown in Figure 8, the increasing flow velocity at the gap outlet leads to a change in the pressure coefficient ($C_p = P/(0.5\rho V_a^2)$) distribution near here. It further changes the distribution of pressure on the propeller surface, which has an effect on the thrust and torque of the propeller. The position of the gap inlet moves downstream as θ increases, and the pressure at the gap inlet increases gradually.

Figure 9 shows 3D pathlines in the gap at different θ with a fixed axial segment length of the gap. For a presentation purpose, only the pathlines passing through four feature points (I, II, III, and IV) are plotted. The four points are uniformly distributed at 30° intervals and are located at the inlet of the gap. The fluid particles at the four points were marked at an initial physical time (t) based on the Lagrangian method. The trajectories of

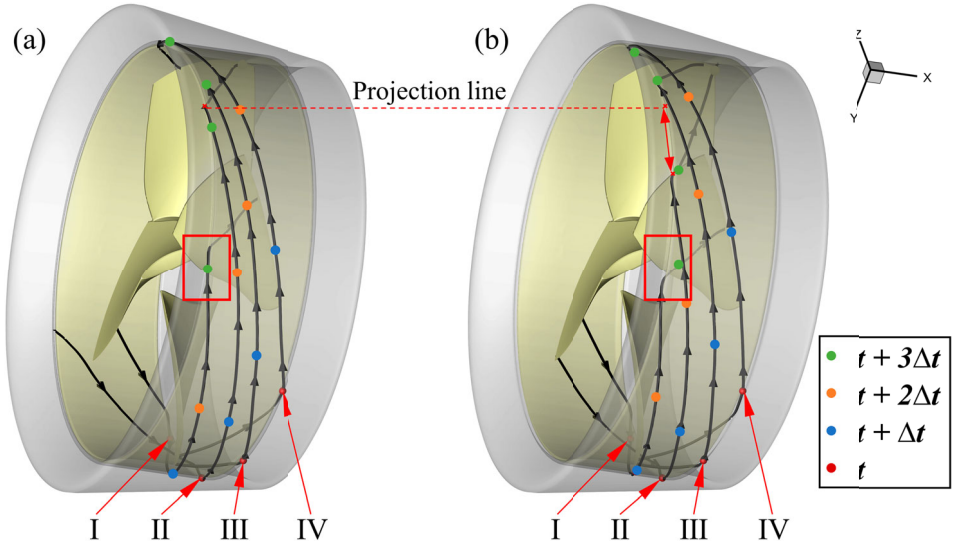

Figure 9. 3D pathlines in the gap at different oblique angles (θ) with a fixed axial segment length of the gap: (a) $\theta = 90°$, and (b) $\theta = 120°$.

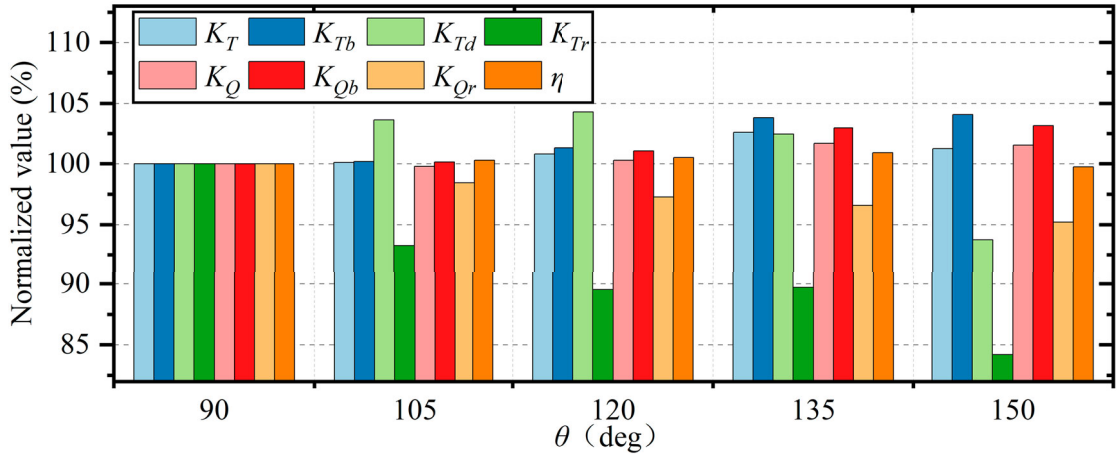

Figure 10. Hydrodynamic characteristics of the RDT at different oblique angles (θ) with the fixed distance between the gap inlet and outlet.

these fluid particles were drawn with the time interval (Δt). As can be seen in Figure 9, the flow is affected by the rotational motion of the propeller and enters the gap with an oblique angle at the entrance. The flow is maintained in the gap in an inclined direction, then exits the gap and is deflected by both the incoming flow and the propeller rotation. It is known that the greater the distance the fluid particles move in the same Δt on the unidirectional pathline, the faster the velocity. When the fluid particles I at $t + 3\Delta t$ are compared in Figures 9a and 9b, it can be seen that the fluid particle with $\theta = 90°$ is still inside the gap, whereas the fluid particle with $\theta = 120°$ has already escaped. Comparing the trajectories of fluid particles II at the gap outlet, it is observed that the fluid particle with $\theta = 120°$ leaves the gap earlier than the one with $\theta = 90°$, and the relative angle between the gap outlet and the inlet is smaller when $\theta = 120°$. This indicates that increasing θ reduces the decelerating effect of the gap corner on the particles, that is, increasing θ is beneficial to the development of the gap flow.

3.2. Fixed distance between the gap inlet and outlet – L_2

Because adjusting the gap inlet and outlet positions does not result in a significant gain in RDT efficiency, this part expands on the previous section by varying the oblique angle and gap axial segment length under the constraint of fixed distance between the gap inlet and outlet. The primary conditions of the numerical simulation are set: $J = 0.5$, $n = 7.5$ rps, and $L_2 = 0.066$ m. Figure 10 illustrates the hydrodynamic characteristics of the RDT at different θ with the fixed distance between the gap inlet and outlet. The improvement in the RDT efficiency can be demonstrated under all working conditions except the maximum angle of 150°. When $\theta = 150°$, both K_T and K_Q enhances, but K_Q enlarges more, resulting in poor efficiency. When θ reaches 120° and 135°, it is accompanied by an increase in K_Q, although K_T increases significantly. The rise in K_T and the drop in K_Q are only obtained when θ is equal to 105°, but the

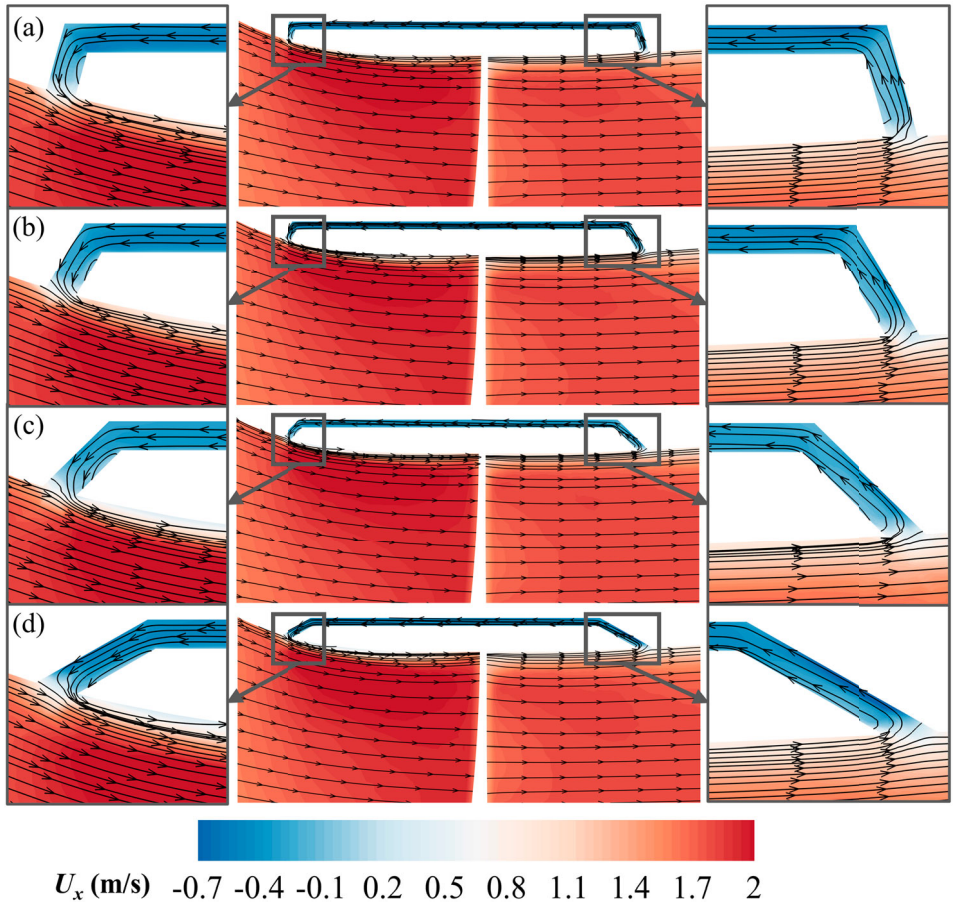

Figure 11. The axial velocity distribution of the flow field at different oblique angles (θ) with the fixed distance between the gap inlet and outlet: (a) $\theta = 105°$, (b) $\theta = 120°$, (c) $\theta = 135°$, and (d) $\theta = 150°$.

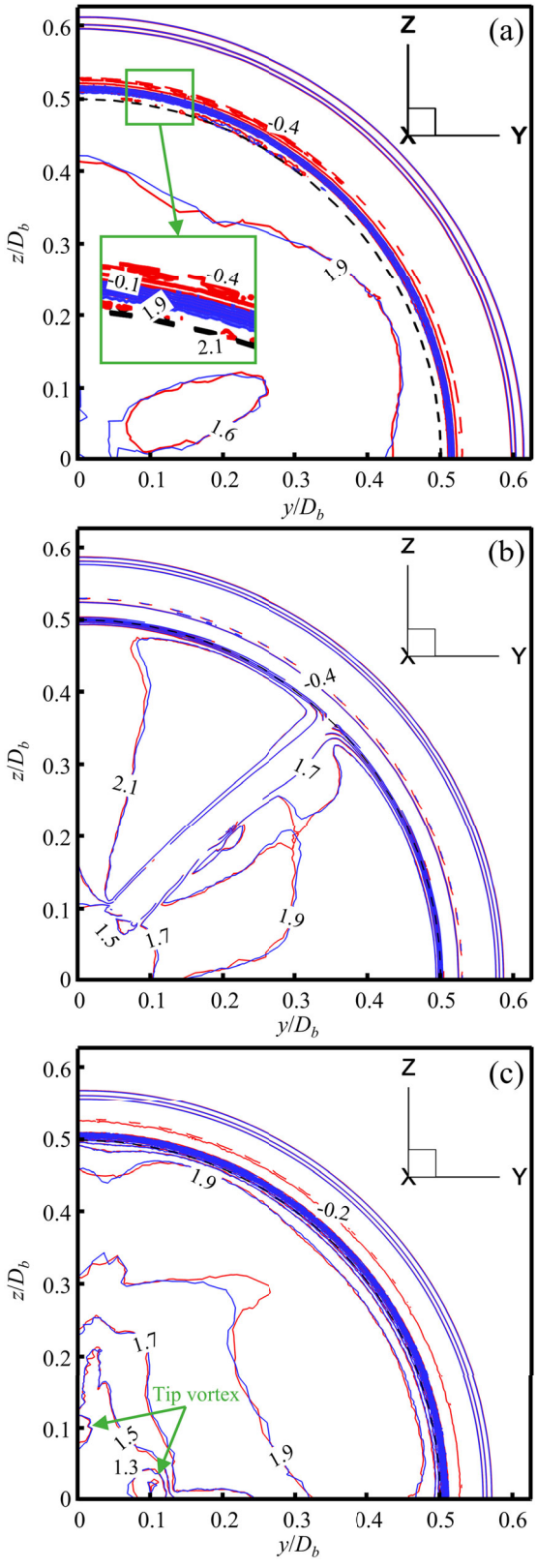

Figure 12. The dimensionless axial velocity contour distribution at different oblique angles ($\theta = 90°$ colored by red and $\theta = 135°$ colored by blue) with the fixed distance between the gap inlet and outlet: (a) cross section A, (b) cross section B, and (c) cross section C.

efficiency gain is limited. The maximum efficiency gain occurs at $\theta = 135°$, which is about 1%. At this point, the K_T increases by approximately 2.6%. The development in θ minimizes the size of the rim, resulting in a reduction in both K_{Tr} and K_{Qr}. It is logical to expect K_{Td} to rise as θ increases, yet it has a tendency to rise and then fall. This phenomenon deserves further discussion in this work.

The axial velocity distribution of the flow field at different θ with the fixed distance between the gap inlet and outlet is presented in Figure 11. Compared with Figure 6, after fixing the inlet and outlet positions of the gap, no small vortex is generated at the entrance of the gap for different θ. The initial inlet and outlet locations of the gap were confirmed to be reasonable.

To further observe the effect of the gap on the flow near the propeller, three cross sections, named section A, B, and C, were cut at the midpoints of the gap outlet ($x/D_b = -0.151$), the propeller disk ($x/D_b = 0$), and the gap inlet ($x/D_b = 0.119$), as shown in Figure 2. Figure 12 displays the axial velocities distribution in the three cross sections at different θ with the fixed distance between the gap inlet and outlet. As a result of the rotation of the blades, there is a certain phase difference in the flow field characteristics of the three cross sections. It is found that the modification of the gap shape influences the axial velocity distribution in sections A and C, while the effect of the gap is difficult to observe in section B owing to the dominance of the rotational motion of the blade. The presence of the gap expands the axial flow rate near the rim, as shown in cross section A. The shedding vortex was observed at the blade tip of the RDT, as shown in cross section C. The vorticity distribution in the wake field at different θ is illustrated in Figure 13. The vortex generated by the blade tip of RDT is well observed and verified. Vortices shedding from the gap and developing along the inner side of the duct to the wake are also observed. The gap vortex leaking out of the gap outlet can be observed in Figure 14. Nonetheless, the differences between the two different θ are very limited. This reflects that the gap oblique angle change has a limited effect on the downstream wake development.

Subsequently, the impacts of different gap shapes are compared by quantitatively analyzing the pressure and velocity variation at the gap inlet and outlet. The locations and angles (φ) of the monitoring points located at the quarter-gap inlet and outlet are displayed in Figure 15. Figure 16 depicts the C_p of the gap inlet and outlet as well as the relative C_p of the two. The varying trends of C_p at different θ are found to be consistent. At the gap outlet, C_p decreases and then increases, reaching the minimum value at the middle of the blade (φ is equal to

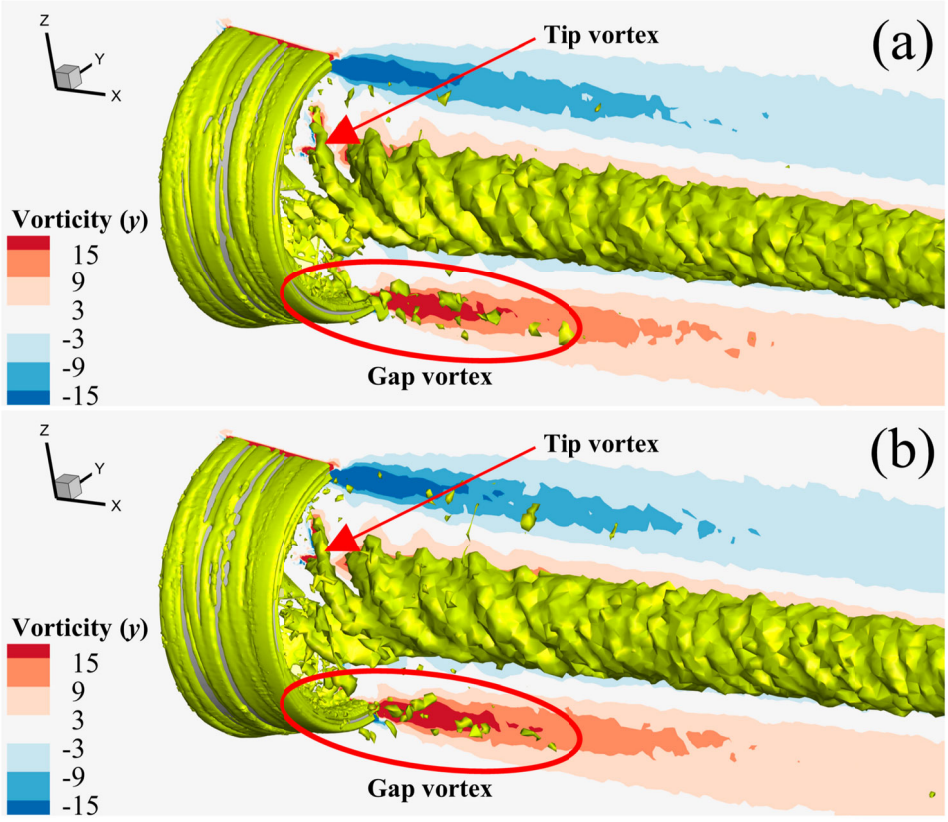

Figure 13. Vortex distribution visualized with an isosurface of the instantaneous Q-criterion in the wake field for the fixed inlet and outlet positions of the gap with different corner angles: (a) $\theta = 90°$, and (b) $\theta = 135°$.

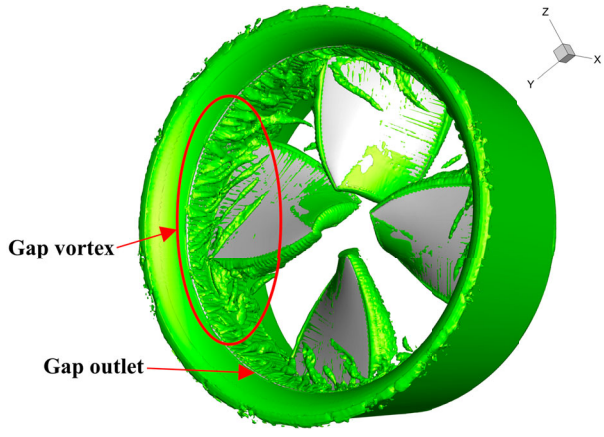

Figure 14. Gap vortex distribution visualized with an isosurface of the instantaneous Q-criterion in the wake field when $\theta = 90°$.

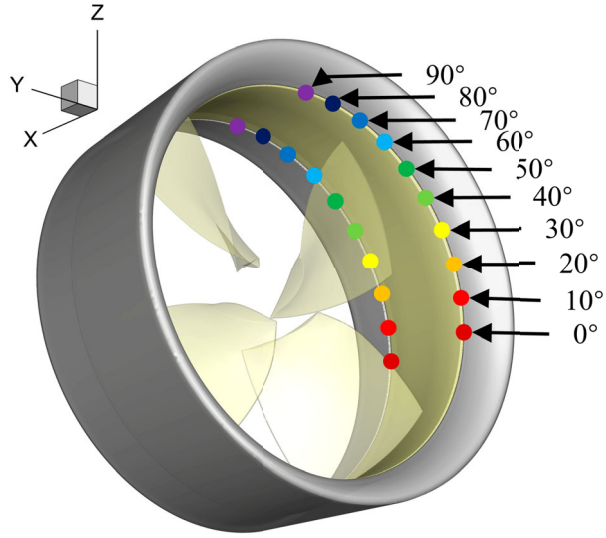

Figure 15. Positions and angles of the monitoring points located at the quarter-gap inlet and outlet.

approximately 45°). At the gap inlet, C_p grows first and then drops, reaching a maximum at $\varphi = 30°$. Since the relative pressure coefficient is the difference between the inlet and outlet, it satisfies the law of first increasing and then decreasing. As can be observed in Figures 16a and b, the C_p at both the gap outlet and inlet grows with increasing θ and decreases beyond $\theta = 135°$. This is in agreement with the trend of efficiency variation of the RDT (see Figure 10), indicating that the change of the gap shape on the pressure is one of the causes of the efficiency variation. As can be noticed in Figure 16c, the relative C_p is lowest at $\theta = 135°$ and largest at $\theta = 150°$. This suggests that reducing the relative pressure at the gap inlet and outlet is beneficial for improving the efficiency of the RDT.

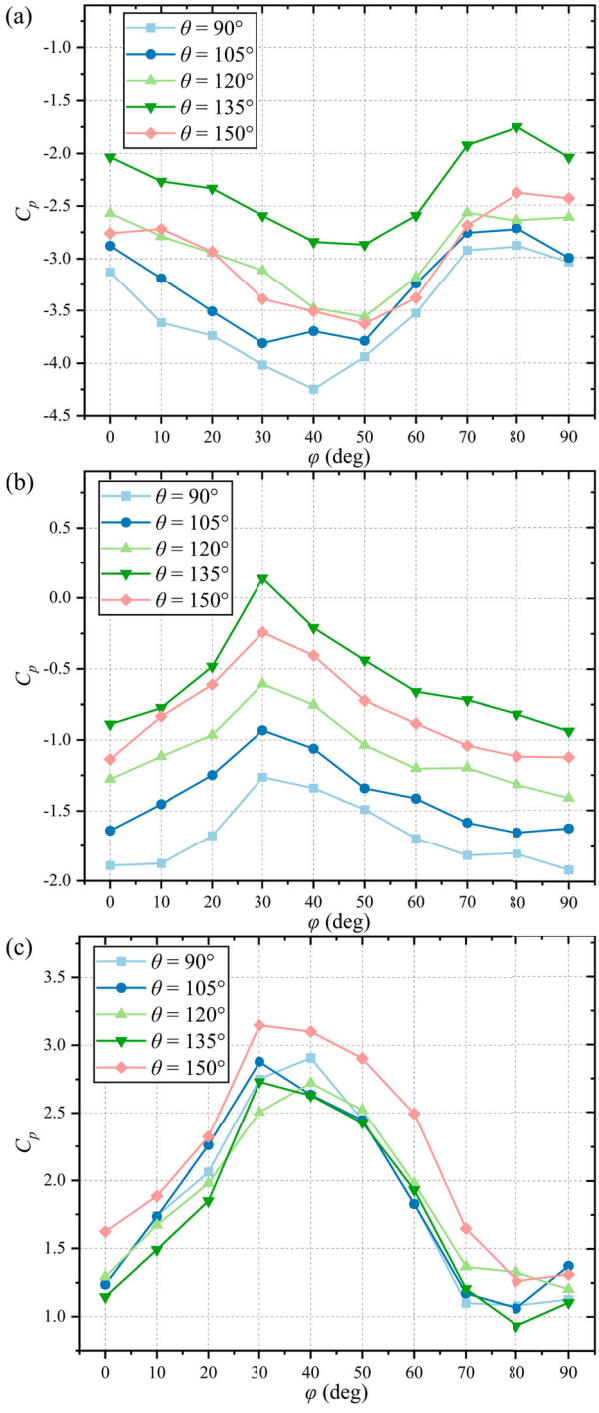

Figure 16. Pressure coefficient (C_p) curves at different monitoring points at different oblique angles (θ) with the fixed distance between the gap inlet and outlet: (a) C_p of the gap outlet, (b) C_p of the gap inlet, and (c) relative C_p between the inlet and outlet of the gap.

Figure 17 compares the value of the difference in pressure coefficients for the results of fixed L_1 (C_{P1}) and fixed L_2 (C_{P2}) at different φ and θ. When $\theta = 90°$, the geometric model is the same, leading to $C_{P1} = C_{P2}$. At the gap outlet, C_{P1} is greater than C_{P2} when θ is equal to 105° and

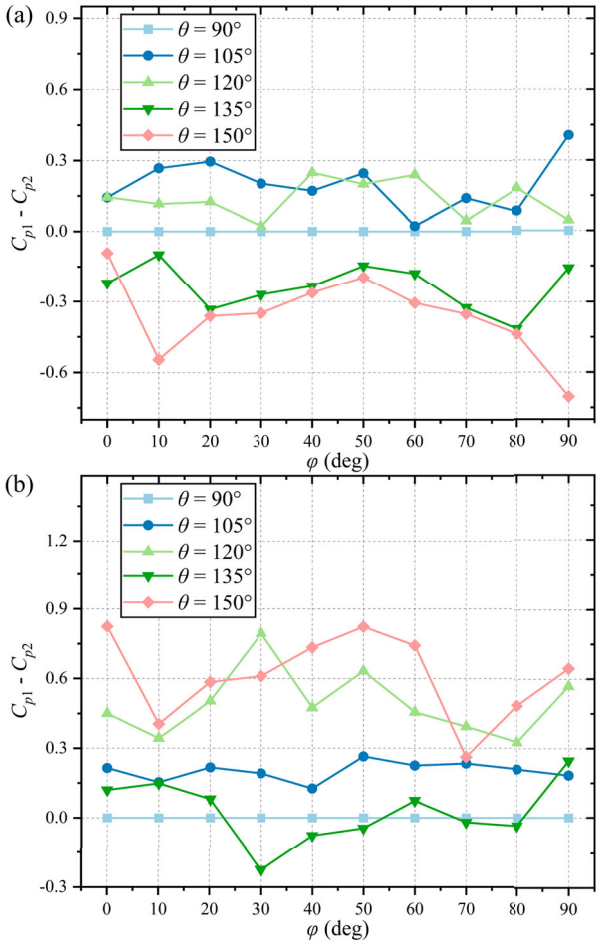

Figure 17. Value of the difference in pressure coefficients for the results of fixed L_1 (C_{P1}) and fixed L_2 (C_{P2}) at different monitoring points at different oblique angles (θ): (a) the gap outlet, and (b) the gap inlet.

120°, while the opposite is true when the θ increases. At the gap inlet, C_{P1} is always larger than C_{P2} except when $\theta = 135°$. The results show that varying the position of the gap inlet and outlet has a significant influence on the pressure distribution when θ is the same.

Figure 18 and Figure 19 demonstrates the flow velocities of different monitoring points at different θ with the fixed distance between the gap inlet and outlet. It is shown that the flow velocities at the gap outlet located in front of the blade is almost unaffected by the propeller rotational flow, while the flow velocities at the gap inlet located behind the blade shows a tendency to rise and then fall. Modifying the gap shape significantly reduces the U_x at the gap outlet, as shown in Figure 18a. When $\theta = 150°$, the U_x curve fluctuates the most, representing the greatest nonuniformity in the flow velocity, which is one of the reasons for the reduced efficiency of this gap shape. The variation pattern of the combined velocity ($U_{yz} = \sqrt{U_y^2 + U_z^2}$) at θ on cross sections is the opposite

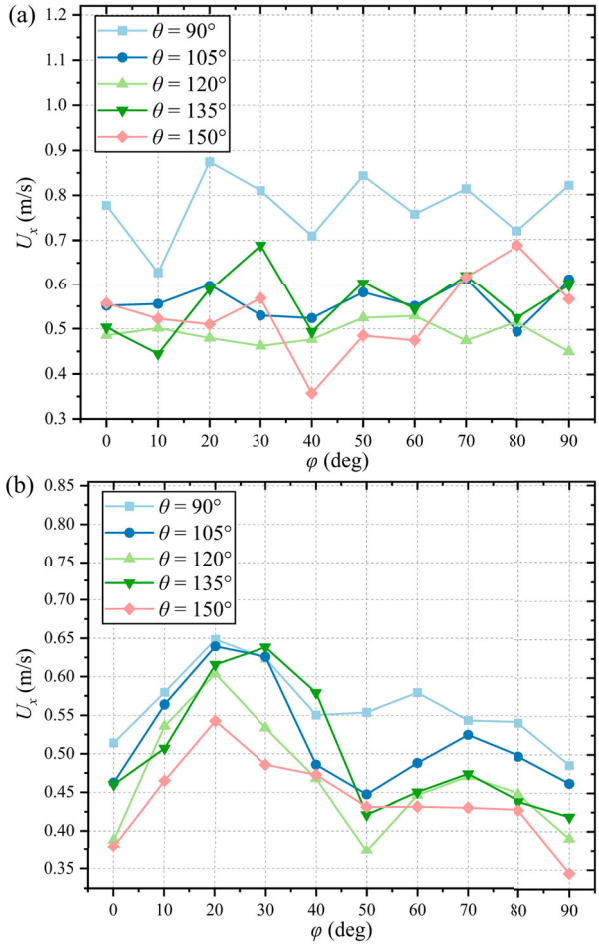

Figure 18. Axial velocities (U_x) of different monitoring points at different oblique angles (θ) with the fixed distance between the gap inlet and outlet: (a) U_x of the gap outlet, and (b) U_x of the gap inlet.

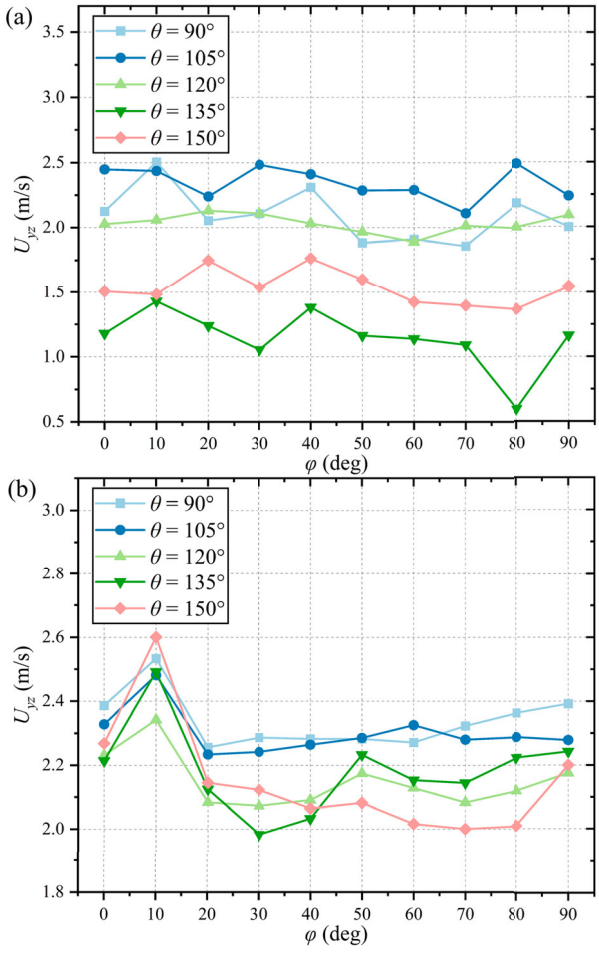

Figure 19. Combined velocities (U_{yz}) of different monitoring points on cross sections at different oblique angles (θ) with the fixed distance between the gap inlet and outlet: (a) U_{yz} of the gap outlet, and (b) U_{yz} of the gap inlet.

of that of K_Q, as shown in Figure 19a and Figure 10. When $\theta = 105°$, U_{yz} is the largest and K_Q is the smallest. As a result, it is suggested that the U_{yz} be increased at the gap outlet in order to reduce the RDT torque.

4. Conclusions and future work

In this study, to investigate the effect of various gap shapes on the hydrodynamic performance of RDT, numerical results based on the OpenFOAM code were compared for the fixed gap axial segment length and the fixed distance between the gap inlet and outlet. The numerical investigation results in the following conclusions:

(1) In the gap, the flow direction is the inverse of the incoming flow direction. The flow enters the gap obliquely from the entrance and is kept inclined in the gap. The increasing flow velocity at the gap outlet has an effect on the thrust and torque of the propeller.

(2) Under the condition of fixed gap axial length, the inlet and outlet positions of the gap are altered by enlarging the θ, but none of the RDT efficiency improvement is obtained. Increasing θ reduces the corner's deceleration effect on the flow, which is useful for gap flow advancement.

(3) Under the condition of fixed inlet and outlet positions of the gap, enhancing the θ can contribute to the improvement of propulsion efficiency. In comparison to the initial model with a gap of $\theta = 90°$, the new gap designs of θ from 105° to 135° improve the efficiency. And $\theta = 135°$ is found to produce the maximum efficiency increase of about 1%.

(4) Reducing the relative pressure at the gap inlet and outlet is beneficial to the RDT's efficiency. One of the causes of efficiency variation is the change in pressure due to gap shape modification. Another reason for the reduced efficiency is nonuniformity in the flow velocity at the gap outlet.

The research of the transient hydrodynamic performance of RDT with gap flow is a complex issue involving the intrinsic mechanism of the vortex structure's influence on the hydrodynamics of unsteady flow fields. To investigate further, consideration of the fluid-solid coupling issue of RDT vibration, ship-RDT interference, cavitation, and noise studies will be necessary. In addition, it is desirable to carry out experimental research on the model-scale and full-scale RDT.

Acknowledgments

The authors would also like to appreciate the Swedish National Infrastructure for Computing (SNIC) for providing computer resources at the Chalmers Centre for Computational Science and Engineering (C3SE).

Disclosure statement

No potential conflict of interest was reported by the author(s).

Funding

This work was supported by the LIGHTHOUSE (Swedish Maritime Competence Center) [grant number FS24_2022/Hållbar sjöfart], and China Scholarship Council [grant number 202106680052].

ORCID

Jianfeng Lin http://orcid.org/0000-0002-0759-8565
Hua-Dong Yao http://orcid.org/0000-0002-9547-7877
Chao Wang http://orcid.org/0000-0001-7855-6939

References

Baltazar, J., Falcão de Campos, J. A. C., & Bosschers, J. (2012). Open-water thrust and torque predictions of a ducted propeller system with a panel method. *International Journal of Rotating Machinery*, *2012*, 1–11. https://doi.org/10.1155/2012/474785

Cao, Q., Hong, F., Tang, D., Hu, F., & Lu, L. (2012). Prediction of loading distribution and hydrodynamic measurements for propeller blades in a rim driven thruster. *Journal of Hydrodynamics*, *24*(1), 50–57. https://doi.org/10.1016/S1001-6058(11)60218-7

Cao, Q., Wei, X., Tang, D., & Hong, F. (2014). Study of gap flow effects on performance of rim driver thrusters. In *Proceedings of the 13th National Conference on Hydrodynamics and the 26th National Symposium on Hydrodynamics*, Tsingtao, China, 1197–1206.

Celik, I. B., Ghia, U., Roache, P. J., & Freitas, C. J. (2008). Procedure for estimation and reporting of uncertainty due to discretization in CFD applications. *Journal of Fluids Engineering*, *130*(7), 078001. https://doi.org/10.1115/1.2960953

Dubas, A. J., Bressloff, N. W., & Sharkh, S. M. (2015). Numerical modelling of rotor–stator interaction in rim driven thrusters. *Ocean Engineering*, *106*, 281–288. https://doi.org/10.1016/j.oceaneng.2015.07.012

Gaggero, S. (2020). Numerical design of a RIM-driven thruster using a RANS-based optimization approach. *Applied Ocean Research*, *94*, 101941. https://doi.org/10.1016/j.apor.2019.101941

Grümmer, H., Harries, S., & Hochbaum, A. C. (2017, June). Simulation-driven Design of a Rim Drive for an Autonomous Vehicle. In *Fifth International Symposium on Marine Propulsors*, Espoo, Finland.

Grűmmer, H. (2016). Design and Optimization of a Hubless rim-driven Thruster for an Autonomous Surface Vehicle using RANSE Simulation (Doctoral dissertation, MS Dissertation, Department of Dynamics of Maritime Systems, Technical University of Berlin, German).

Hu, J., Yan, Q., Ding, J., & Sun, S. (2022). Numerical study on transient four-quadrant hydrodynamic performance of cycloidal propellers. *Engineering Applications of Computational Fluid Mechanics*, *16*(1), 1813–1832. https://doi.org/10.1080/19942060.2022.2118171

Jiang, H., Ouyang, W., Sheng, C., Lan, J., & Bucknall, R. (2022). Numerical investigation on hydrodynamic performance of a novel shaftless rim-driven counter-rotating thruster considering gap fluid. *Applied Ocean Research*, *118*, 102967. https://doi.org/10.1016/j.apor.2021.102967

Kort, L. (1940). Elektrisch angertriebene schiffsschraube. *German Patent*, *688*(114), 13.

Lea, M., Thompson, D., Blarcom, B., Eaton, J., Friesch, J., & Richards, J. (2003). Scale model testing of a commercial rim-driven propulsor pod. *Journal of Ship Production*, *19*(02), 121–130. https://doi.org/10.5957/jsp.2003.19.2.121

Lin, J., Guo, C., Zhao, D., Han, Y., & Su, Y. (2022a). Hydrodynamic simulation for evaluating Magnus anti-rolling devices with varying angles of attack. *Ocean Engineering*, *260*, 111949. https://doi.org/10.1016/j.oceaneng.2022.111949

Lin, J., Han, Y., Guo, C., Su, Y., & Zhong, R. (2022b). Intelligent ship anti-rolling control system based on a deep deterministic policy gradient algorithm and the Magnus effect. *Physics of Fluids*, *34*(5), 057102. https://doi.org/10.1063/5.0089697

Lin, J., Zhao, D., Guo, C., Zhang, Z., & Su, Y. (2020). Numerically modeling the effect of flexibility on flow around marine engineering structures: Using the shape of the Saguaro Cactus. *Journal of Coastal Research*, *36*(3), 628–635. https://doi.org/10.2112/JCOASTRES-D-19-00115.1

Liu, B., & Vanierschot, M. (2021). Numerical study of the hydrodynamic characteristics comparison between a ducted propeller and a rim-driven thruster. *Applied Sciences*, *11*(11), 4919. https://doi.org/10.3390/app11114919

Liu, B., Vanierschot, M., & Buysschaert, F. (2022a, August). Comparison study of the k − kL − ω and γ − Reθ transition models in the open water performance prediction of a rim-driven thruster. In *Conference on Modelling Fluid Flow (CMFF'22)*, Budapest, Hungary, 70–77.

Liu, B., Vanierschot, M., & Buysschaert, F. (2022b). Effects of transition turbulence modeling on the hydrodynamic performance prediction of a rim-driven thruster under different duct designs. *Ocean Engineering*, *256*, 111142. https://doi.org/10.1016/j.oceaneng.2022.111142

Menter, F. R., Kuntz, M., & Langtry, R. (2003). Ten years of industrial experience with the SST turbulence model. *Turbulence, Heat and Mass Transfer*, *4*(1), 625–632.

Ottersten, M., Yao, H., & Davidson, L. (2022a). Inlet gap effect on aerodynamics and tonal noise generation of a voluteless centrifugal fan. *Journal of Sound and Vibration*, *540*(8), 117304. https://doi.org/10.1016/j.jsv.2022.117304

Ottersten, M., Yao, H., & Davidson, L. (2022b). Inlet gap influence on low-frequency flow unsteadiness in a centrifugal fan. *Aerospace*, *9*(12), 846. https://doi.org/10.3390/aerospace9120846

Shao, X., Santasmasas, M. C., Xue, X., Niu, J., Davidson, L., Revell, A. J., & Yao, H. (2022). Near-wall modeling of forests for atmosphere boundary layers using lattice Boltzmann method on GPU. *Engineering Applications of Computational Fluid Mechanics*, *16*(1), 2143–2156. https://doi.org/10.1080/19942060.2022.2132420

Song, B., Wang, Y., & Tian, W. (2015). Open water performance comparison between hub-type and hubless rim driven thrusters based on CFD method. *Ocean Engineering*, *103*, 55–63. https://doi.org/10.1016/j.oceaneng.2015.04.074

Song, K., Guo, C., Sun, C., Wang, C., Gong, J., Li, P., & Wang, L. (2021). Simulation strategy of the full-scale ship resistance and propulsion performance. *Engineering Applications of Computational Fluid Mechanics*, *15*(1), 1321–1342. https://doi.org/10.1080/19942060.2021.1974091

Song, X., Zhao, G., Yuan, L., Yang, B., Tian, G., & Ai, X. (2020). Numerical research of hydrodynamic performance impact factors of rim-driven thruster. *Ship Engineering*, *42*(7), 67–71+163. https://doi.org/10.13788/j.cnki.cbgc.2020.07.13

Su, Y., Lin, J., Zhao, D., Guo, C., Wang, C., & Guo, H. (2020). Real-time prediction of large-scale ship model vertical acceleration based on recurrent neural network. *Journal of Marine Science and Engineering*, *8*(10), 777. https://doi.org/10.3390/jmse8100777

Yakovlev, A. Y., Sokolov, M. A., & Marinich, N. V. (2011, June). Numerical design and experimental verification of a rim-driven thruster. In *Proceedings of Second International Symposium on Marine Propulsors*, Hamburg, Germany, 396–403.

Yan, X., Liang, X., Ouyang, W., Liu, Z., Liu, B., & Lan, J. (2017). A review of progress and applications of ship shaftless rim-driven thrusters. *Ocean Engineering*, *144*, 142–156. https://doi.org/10.1016/j.oceaneng.2017.08.045

Yao, H., & Davidson, L. (2019). Vibro-acoustics response of a simplified glass window excited by the turbulent wake of a quarter-spherocylinder body. *The Journal of the Acoustical Society of America*, *145*(5), 3163–3176. https://doi.org/10.1121/1.5109548

Zhai, S., Jin, S. B., Chen, J. Q., Liu, Z. H., & Song, X. L. (2022). CFD-based multi-objective optimization of the duct for a rim-driven thruster. *Ocean Engineering*, *264*, 112467. https://doi.org/10.1016/j.oceaneng.2022.112467

Zhu, Z. P., & Liu, H. L. (2022). The external characteristics and inner flow research of rim-driven thruster. *Advances in Mechanical Engineering*, *14*(2), 168781322210816. https://doi.org/10.1177/16878132221081608